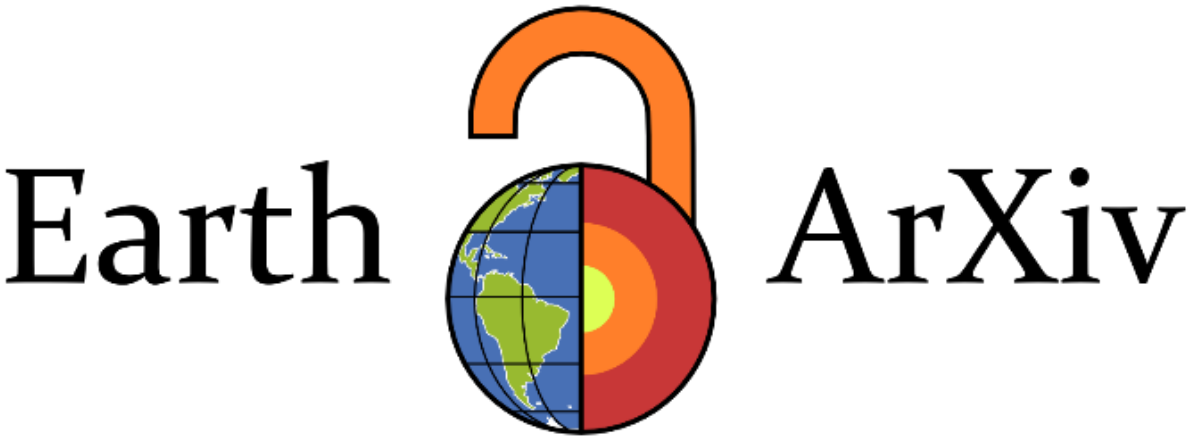

Anomaly detection of Synthetic Aperture Radar Interferograms with semi-supervised machine learning

Estibaliz Martinez[1], **Yosuke Aoki**[1]

[1]Earthquake Research Institute, The University of Tokyo, Tokyo, Japan

Key Points:

- We developed a method to detect subtle deformation signals from a SAR interferogram.
- Our method is based on the probability distribution of the data and does not require an external training dataset.
- We confirmed the applicability of the method with real datasets.

Corresponding author: Yosuke Aoki, yaoki@eri.u-tokyo.ac.jp

Corresponding author: Estibaliz Martinez, estibalizm@g.ecc.u-tokyo.ac.jp

Abstract

The aim of this research is to detect Earth's deformation from Interferometric Synthetic Aperture Radar (InSAR) images through a semi-supervised machine learning algorithm called Least-Squares Two-sample Test (LSTT). This algorithm computes the probability distributions of two samples to assess if they belong to the same probability distribution. At the same time, it gives the divergence of these two samples. Therefore, discrimination of noise and deformation signals requires comparing the probability distribution of the samples. Our method is tested with two different datasets obtained from the ALOS-2 satellite. One is the deformation of the 2020 Taal volcano, Philippines, eruption. The other is the deformation due to the gas extraction in the Boso Peninsula, Japan, between 2017 and 2018. The first one shows obvious deformation, while the second presents a less visible deformation. Our method, tested with the Receiver Operating Characteristic curve, mostly detected the deformation correctly as an anomaly, regardless of how visually obvious the deformation is. However, our method can sometimes lead to a biased prediction when the noise level is high.

Plain Language Summary

The goal of this study is to figure out how to objectively detect changes happening on Earth's surface from Synthetic Aperture radar images. To meet this goal, we developed a method to detect the surface deformation as an anomaly. To test our method, two different events have been studied. The first event is a volcanic eruption in the Philippines, where the deformation of the Earth is clearly visible. The second is a land subsidence due to gas extraction in Japan, in which the deformation is less significant. The results show that our method accurately detects the deformation as an anomaly, regardless of how obvious the deformation is. We demonstrate the utility of our method to understand when and where the Earth's surface is deformed. However, our method sometimes does not work well when the noise level in the radar images is high.

1 Introduction

Synthetic Aperture Radar (InSAR) has been a fundamental tool for measuring Earth's surface deformation since its emergence in the 1990s (e.g., Burgmann et al., 2000; Simons & Rosen, 2015). The deformation has been most traditionally measured through interferometry of SAR images (Interferometric Synthetic Aperture Radar; InSAR). InSAR

has detected Earth's surface deformation associated with various phenomena, including tectonic (e.g., Weiss et al., 2020), volcanic (e.g., Hooper et al., 2012; Pinel et al., 2014), and hydrological (e.g., Morishita, 2021; Shirzaei et al., 2020) activity, with its unprecedented spatial resolution.

Despite its utility, InSAR has weaknesses, as with every geodetic technique. One of them is the higher noise level than other geodetic techniques, such as the Global Navigation Satellite System (GNSS). The main sources of noise in InSAR images are ionospheric and atmospheric disturbances of microwaves radiated from a SAR satellite. GNSS measurements can get rid of the effect of ionospheric disturbance because a GNSS satellite radiates multiple frequencies of microwaves, and the ionospheric effect is frequency-dependent. On the other hand, InSAR measurements cannot remove the ionospheric disturbance as the GNSS observations do because a SAR satellite radiates only a single frequency of microwave. InSAR measurements are also more susceptible to atmospheric disturbance than GNSS measurements. While the atmospheric disturbance of GNSS measurements can be evaluated from measurements over time, that of SAR measurements needs to be evaluated from instantaneous observations. Therefore, uncertainties of InSAR measurements are generally higher than GNSS measurements; the perturbations described above mask small signals in SAR interferograms. The spatial correlation of ionospheric and atmospheric disturbances makes discriminating the deformation signal from noise even more challenging.

If a large number of interferograms is available, removing the ionospheric and atmospheric disturbance is possible through the time-series analysis (e.g., Hooper et al., 2012; Morishita et al., 2020; Schmidt & Bürgmann, 2003) by taking advantage that they are spatially correlated but temporally uncorrelated. However, temporal smoothing in time-series analysis can make small and short-lived deformation signals. This study, instead, attempts to develop a method to detect deformation signals from a single interferogram rather than relying on multiple interferograms.

To achieve this goal, several studies have taken machine-learning approaches to automatically detect deformation signals from a single interferogram. For example, Brengman & Barnhart (2021) and Anantrasirichai et al. (2019) developed a method to detect volcano deformation signals with Convolution Neural Network (CNN). As the training dataset, they generated interferograms from synthetic pressure sources to compensate

for an insufficient number of observations as the training dataset. Such supervised learning with a synthetic dataset can detect only the deformation of known origins. In other words, such an approach does not help detect deformation of unknown origin, or discover new phenomena. Additionally, Beker et al. (2023) detected subtle volcanic deformations applying AI tools, and a CNN trained on synthetically generated deformation data. But to mitigate the problem of not having real data and improve the performance, the fine-tuning stage is developed with a small real dataset. Popescu et al. (2025) proposed another study to detect volcanic deformation applying CNN as well as two generative models, but in this approach, it avoids the need for labeled training data. However, it still involves complex deep architectures and volcano-specific tuning. Gaddes et al. (2024) employed 500,000 labeled interferograms as the training dataset. However, this training dataset is solely for volcanic deformation. Another dataset is required to train more generic deformation patterns.

To circumvent this problem, we developed a method to detect deformation signals, or anomalies, from a single InSAR image. A main assumption of our method is that an interferogram is dominated by regions of no deformation anomalies. While some interferograms contain deformation signals in the whole image, these images are out of the scope of our study because even visual inspection allows us to detect anomalies in such images.

Our method is verified by applying it to two datasets taken from the ALOS-2 satellite, one associated with the 2020 Taal Volcano, Philippines, eruption, and the other associated with land subsidence in the Boso Peninsula, Japan. Because ground deformation by the 2020 Taal volcano eruption is visible even with visual inspection (Bato et al., 2021), the application of our method to this dataset serves as the validation of it. On the other hand, land subsidence in the Boso Peninsula is not necessarily visible from a single interferogram because the subsidence there is only up to a few tens of millimeters per year (Kinoshita & Furuta, 2024; Nonaka et al., 2020). The application of our method to this dataset confirms that it works for detecting deformation signals that are not detectable by visual inspection.

2 Method

We detect anomalies in an interferogram by examining the probability distribution of the data. The first assumption of our method is that the data in a subregion of an undeformed interferogram gives similar probability distributions between different subregions. In other words, we assume a spatially uniform noise structure within an interferogram. The second assumption is that anomalies are only in a small fraction of the image, if any. Therefore, the ground deformation in a deformed region is detected as a probability distribution anomaly from much of the data.

To meet the two assumptions above, we employed the Least-Squares Two-Sample test (LSTT; Sugiyama et al., 2011) to detect an anomaly of deformation signals as an anomalous probability distribution of the data. LSTT, a non-parametric method, tests if two data samples are drawn from the same underlying probability distribution. Two samples without deformation signals give statistically similar probability distributions. Otherwise, the two probability distributions are considered to be drawn from two different underlying probability distributions. LSTT does not require any restrictive parametric assumptions in deriving the density ratio between two probability distributions. Specifically, LSTT is based on a divergence density ratio estimation method called unconstrained least-squares importance fitting (uLSIF). LSTT employs uLSIF because of the enhanced computational efficiency by processing the data sample only through kernel functions. The Gaussian kernel function helps to create a linear classifier of a nonlinear decision boundary dataset.

The probability density ratio $r(\mathbf{x})$ between two probability distributions $p(\mathbf{x})$ and $p(\mathbf{x}')$ is represented as $r(\mathbf{x}) = p(\mathbf{x})/p(\mathbf{x}')$. uLSIF estimates $r(\mathbf{x})$, with $p(\mathbf{x}') \geq 0$. Then, a kernel

$$k(\mathbf{x}, \mathbf{x}') = \exp\left(-\frac{\|\mathbf{x} - \mathbf{x}'\|}{2\sigma^2}\right) \tag{1}$$

is introduced to improve the accuracy of the estimated $r(\mathbf{x})$ (Sugiyama et al., 2011). In equation (1), the norm is Euclidean, and σ^2 denotes variance representing the characteristic kernel width. The performance of uLSIF resides in the choice of σ^2. See Sugiyama et al. (2011) for the method of finding the optimal value of σ to make LSTT a non-parametric method.

The obtained ratio estimation substitutes the initial density ratio in the Pearson divergence estimator (Equation 2) to obtain the desired estimator for the uLSIF func-

tion. Next, the elements of the union of the two datasets, $\mathbf{x} \cup \mathbf{x}'$, are randomly permuted so that the first N elements consist of a set $\tilde{\mathbf{x}}$ and the remaining samples the set $\tilde{\mathbf{x}'}$, where N denotes the length of $\mathbf{x}$. We then shuffled the union elements, $\tilde{\mathbf{x}} \cup \tilde{\mathbf{x}'}$, and compute Pearson divergence, $PE(\tilde{\mathbf{x}}||\tilde{\mathbf{x}'})$, 100 times. We finally compare these estimator with those from the original dataset.

$$PE(p(\mathbf{x})||p(\mathbf{x}')) = \int_{-\infty}^{\infty} p(\mathbf{x}') \cdot \left(\frac{p(\mathbf{x})}{p(\mathbf{x}')} - 1 \right)^2 d\mathbf{x} \tag{2}$$

To test the algorithm described above, four sets of data samples are taken from the filtered interferogram. Two of them are associated with areas where the displacement is obvious. We use the measure of the p-value for hypothesis testing. When we compare two samples, the p-value indicates the probability that these samples are taken from different probability distributions. In other words, the Pearson divergence between samples with clear deformation signals should be significantly greater than zero, while the p-value should be close to 0 to reject the null hypothesis. Additionally, the other two samples correspond to similar regions with a p-value close to 1. **Fig. 1** graphically depicts pairs of with p-values close to 0 and 0.9. To summarize, this measure helps us see if the apparent difference between two datasets is due to random sampling or statistically significant.

We compared the two probability distributions of the Laplacian of the line-of-sight (LOS) distance changes rather than the LOS distance changes themselves. The idea behind this implementation is that an anomalous interferogram, or an interferogram with deformation signals, has different spatial roughness from that without deformation signals.

The Laplacian of the LOS displacements ϕ is represented as

$$\nabla^2 \phi = \frac{\partial^2 \phi}{\partial x^2} + \frac{\partial^2 \phi}{\partial y^2} \tag{3}$$

where x and y denote perpendicular directions on the interferogram, e.g., the east and north directions, respectively. The discretized form of Laplacian is given by

$$\nabla^2 \phi_{i,j} = \frac{\phi_{i+1,j} - 2\phi_{i,j} + \phi_{i-1,j}}{\Delta x^2} + \frac{\phi_{i,j+1} - 2\phi_{i,j} + \phi_{i,j-1}}{\Delta y^2} \tag{4}$$

where $\phi_{i,j}$, Δx, and Δy denote the LOS change at the (i, j) grid, the spacing of the data in the x direction, and that in the y direction, respectively. When $\Delta x = \Delta y$, equation

(a) Different distributions, p-value ≈ 0.00 (b) Similar distributions, p-value ≈ 0.9

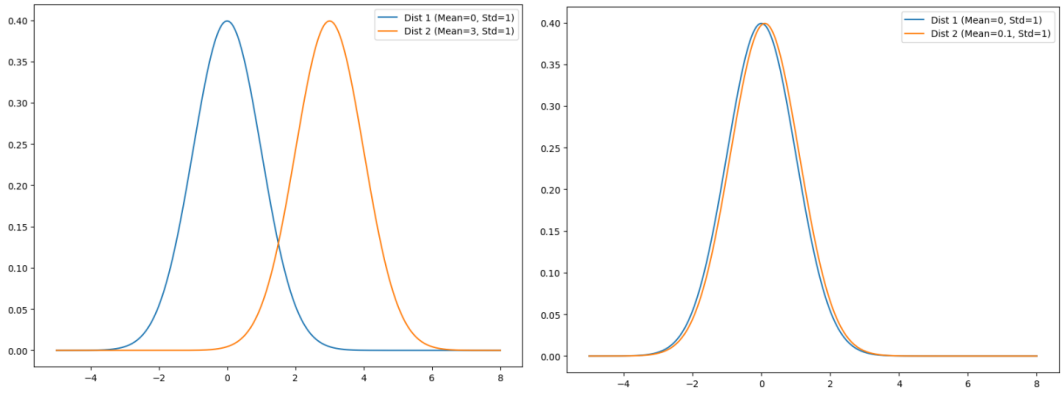

Figure 1: Comparison of normal probability distribution functions (PDFs) generated with synthetic data. The image (a) depicts two distinct PDFs, while (b) illustrates nearly identical PDFs. Both images display the distribution of the values that the function takes along the x-axis and their corresponding probability densities along the y-axis.

(4) is simplified as

$$\nabla^2 \phi_{i,j} = \frac{-4\phi_{i,j} + \phi_{i+1,j} + \phi_{i-1,j} + \phi_{i,j+1} + \phi_{i,j-1}}{\Delta x^2}. \tag{5}$$

The discrete form of the Laplacian, instead of the continuous one, has been used because the pixel values of the InSAR images can be identified easily as a discrete grid. In addition, if we take as an input two samples, they will be treated as equal although they are clearly not. So the use of the discrete Laplace operator as a proxy of spatial smoothness is the key to make the algorithm correctly interpret the data.

3 Data

3.1 InSAR images

An InSAR image is constructed from two SAR images. A SAR image is a two-dimensional record; Each pixel consists of a complex number with amplitude, representing the strength of the reflected signal, and phase, representing the distance between the satellite and the target (ground). The phase difference between the two SAR images reveals ground deformation after appropriate corrections. In a word, it is the phase difference that enables us to measure the deformation of the Earth's surface (Burgmann et al., 2000).

This study applies our method to two SAR interferograms; one is ground deformation associated with the 2020 Taal, Philippines, volcano eruption and the other is associated with ground subsidence in the Boso Peninsula, Japan, between 2017 and 2018, both taken from the ALOS-2 satellite. Both interferograms contain deformation signals only in a part of the interferogram, and a part of the interferogram is free of deformation signals.

3.1.1 The 2020 eruption of Taal volcano, Philippines

Taal volcano is one of the most active volcanoes in the Philippines. The most recent eruption was in 2020 after 43 years of dormancy. The 2020 eruption was a phreatomagmatic explosion with an ash column of 16–17 km by an interaction of magma and the water of Taal Lake, the caldera lake of Taal volcano (Balangue-Tarriela et al., 2022; Perttu et al., 2023).

The 2020 eruption of Taal volcano generated significant ground deformation. Bato et al. (2021) processed ALOS-2 images spanning the eruption to show that the eruption generated line-of-sight displacements of up to 2 meters. They explained the observed displacements by a mass loss from the magma reservoir at a depth of 5 km by $\sim 0.5\text{km}^3$ and a lateral dike intrusion by $\sim 0.6\text{km}^3$.

Fig.2 shows an example of interferogram representing the co-eruptive deformation. This interferogram shows the change of line-of-sight distances, which is from the west-southwest. the subsidence and east-northeastward displacements correspond to the line-of-sight extension while the uplift and west-southwestward displacements correspond to the line-of-sight contraction. Consequently, solely this interferogram cannot distinguish between the subsidence and east-northeastward displacements or uplift and west-southwestward displacements.

The co-eruptive deformation is concentrated around the vent or the southwestern part of **Fig.2**. Spatial variations of line-of-sight displacements in other regions are due mainly to atmospheric disturbance (e.g., Massonnet et al., 1994; Zebker et al., 1997) rather than real surface displacements. Also, because InSAR cannot measure surface displacement offshore, no measurements are available at Lake Taal and Laguna de Bay (**Fig.2**).

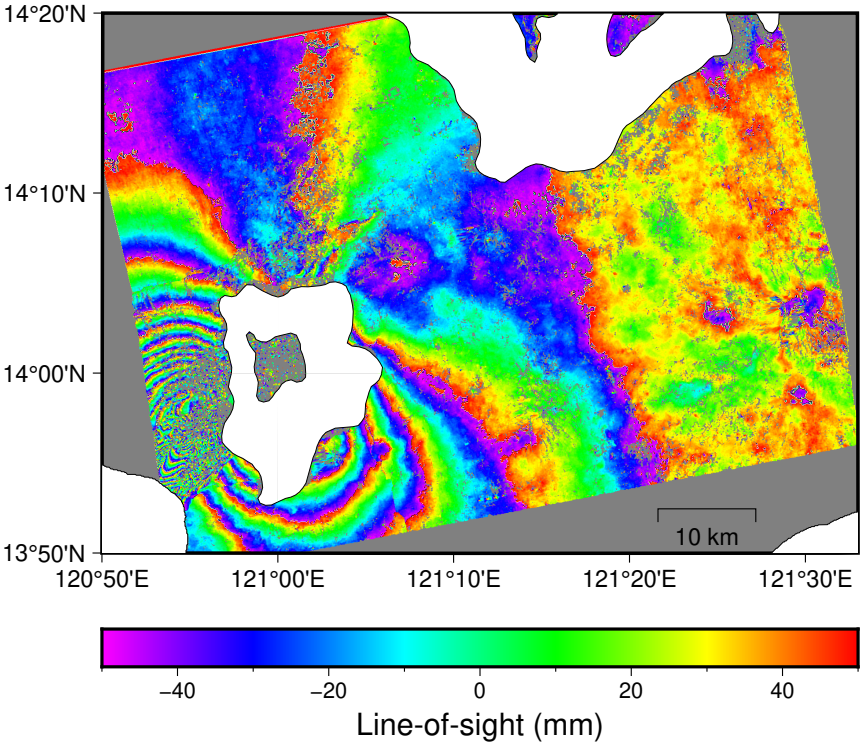

Figure 2: Line-of-sight changes associated with the 2020 eruption of Taal Volcano between 12 November 2019 and 21 January 2020, spanning the eruption on 12 January 2020. SAR images are taken from the ascending orbit, and the line-of-sight is roughly from the west-southwest. The interferogram is unwrapped and rewrapped every 100 mm.

3.1.2 Subsidence of the Boso Peninsula, Japan

Boso Peninsula is located to the east of the Tokyo Metropolitan area. Excessive extraction of natural gas has subsided a part of the peninsula by up to 10 mm/yr in the past few decades (Furuno et al., 2015; Nonaka et al., 2020). Also, deformation by quasi-periodic slow slips (e.g., Fukuda, 2018; Ozawa et al., 2019; Kinoshita & Furuta, 2024) can contaminate interferograms in the southeastern Boso Peninsula.

Fig.3 depicts the deformation between 9 March 2017 and 15 November 2018. Although the interferogram is dominated by a long-wavelength feature, it shows the line-of-sight extension, or subsidence, in the northern tip and the middle of the peninsula. In addition, the long-wavelength deformation due to the convergence of the Philippine Sea plate from the south and the postseismic deformation of the 2011 Tohoku-oki earthquake (Mw=9.0), whose epicenter is ∼300 km to the north, might contaminate the dis-

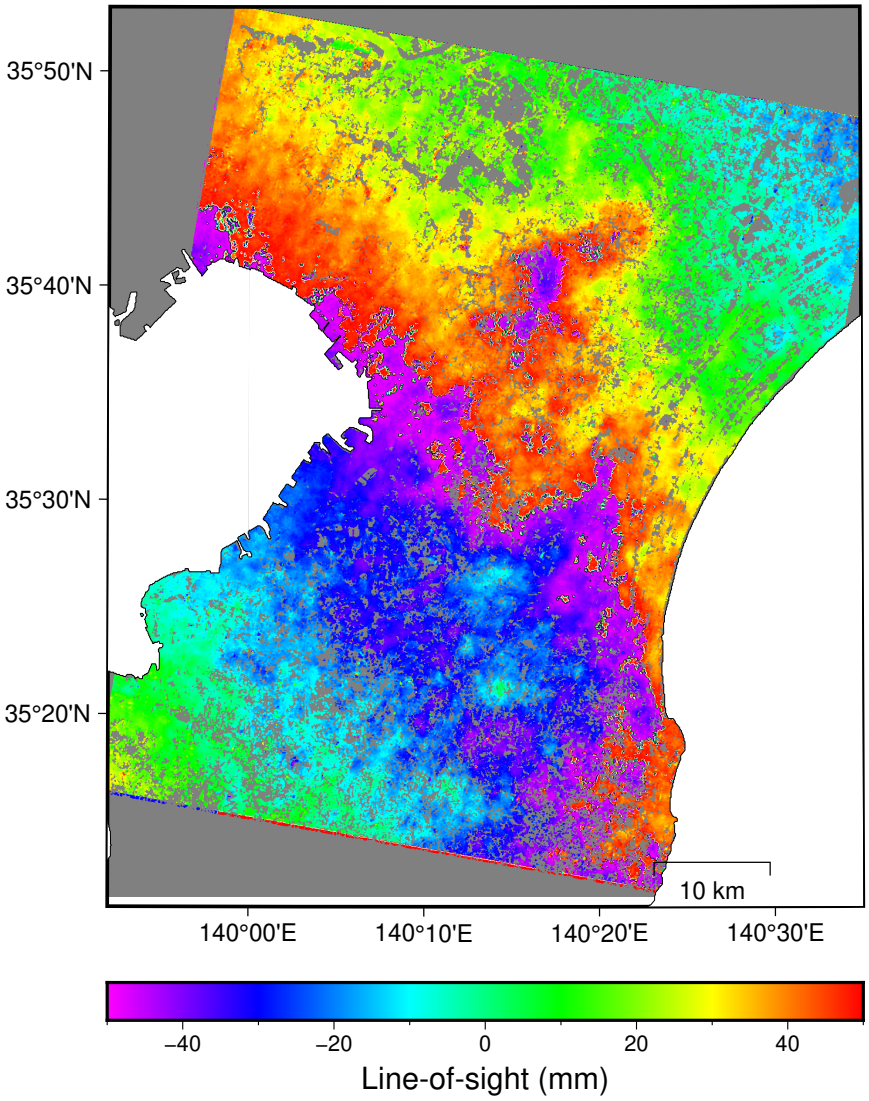

Figure 3: Line-of-sight changes in Boso Peninsula between 9 March 2017 and 15 November 2015. SAR images are taken from the descending orbit, and the line-of-sight is roughly from the east-southeast. The interferogram is unwrapped and rewrapped every 100 mm.

placement field. Because the strain rate by the plate convergence is on the order of 10^{-7} (e.g., Kato et al., 1998; Sugiyama et al., 2011; Okazaki et al., 2021), the relative displacement between both ends of the image separated by ∼50 km is about ∼5 km.

Also, postseismic deformation of the 2011 Tohoku-oki earthquake (Mw=9.0) and a slow-slip transient in June 2018 to the southeast of the Boso Peninsula (e.g., Kinoshita and Furuta, 2024)

3.2 Data Processing

The data processing is done by the GMTSAR software (Sandwell et al., 2011). The processing follows the standard InSAR processing; the interferogram of co-registered images is further processed by removing the orbital and topographic phases to extract ground deformation between the two acquisitions. The Digital Elevation Map with a resolution of 1 arc seconds, or about 30 meters, from Shuttle Radar Topography Mission 1 (Farr et al., 2007) and that with a resolution of 0.4 arc seconds, or about 10 meters, from Geospatial Information Authority are used to correct the topographic effect in the Taal and Boso cases, respectively.

In the Taal case, the SAR images are acquired on 12 November 2019 and 21 January 2020, spanning the eruption on 12 January 2020. In the Boso case, we processed SAR images acquired on 9 March 2017 and 15 November 2018. The obtained displacements with a coherence greater than 0.1 is considered reliable observations and left for the subsequent anomaly detection analysis.

Once processing is finished, the resulting data (interferogram and coherence file) is read and filtered. In order to do this, a Python script (v.3.13.5) was written and executed through IDLE. The obtained coherence file has the information about the quality of the interferogram. Consequently, the InSAR image is filtered using a threshold coherence of 0.1, which means that all values of the interferogram smaller or equal to 0.1 were discarded and substituted by NaN. The interferogram units are radians so to converted it to a standard unit (mm), it is mandatory to use the following equation $118/2\pi \times 1847 \times 1769$, where 1847×1769 are the dimensions of the Taal interferogram. Similarly, 6777×6315 are the dimensions of the Boso InSAR image.

Lastly, the algorithm was implemented in Python (v.3.13.5) and executed in a Jupyter Notebook environment. Experiments were conducted on a MacBook Pro equipped with an Apple M3 Pro chip (11-core CPU: 5 performance cores and 6 efficiency cores), 18GB of unified memory, and macOS Sequoia 15.5. The implementation relied on Numpy (v.2.3.0) and SciPy (v.1.15.3). The code was executed on CPU only, and the average runtime over 200 runs was 1.8763 seconds with a $\pm$ 0.1043 seconds standard deviation, indicating stable execution performance. Although the algorithm was tested on two different datasets, the average runtime reported refers specifically to the Boso Peninsula data, as the variation across datasets was negligible.

4 Results

In the **Fig.4**, it can be observed that for 100 iterations of the algorithm, the obtained values for different samples are clearly close to 0, while for similar samples the values are more evenly distributed with a mean of 0.4. We understand by similar samples those obtained from similar probability distributions, in the same way as we call different samples those derived from distinct probability distributions.

(a) Taal InSAR data

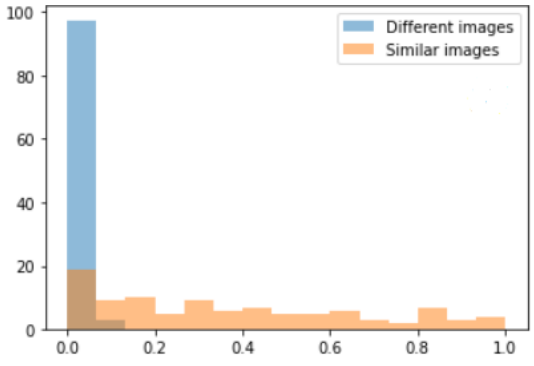

(b) Boso InSAR data

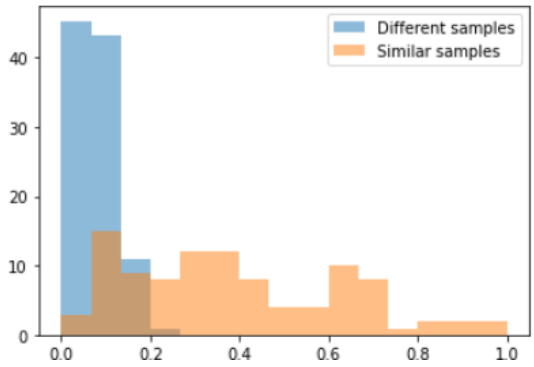

Figure 4: Histogram showing the comparison of the distribution of p-values generated after 100 iterations of the LSTT algorithm for different samples (blue) and for similar samples (orange) for the Taal InSAR image (a) and the Boso InSAR image (b). It showcase the frequency (on the y-axis) at which specific p-values (on the x-axis) occur.

Furthermore, the true positive (TP), true negative (TN), false positive (FP) and false negative (FN) have been computed with a threshold of 0.1, resulting in 99% TP, 25% FP, 74% TN and 1% FN for the Taal data. Meanwhile, 69% TP, 7% FP, 93% TN and 26% FN for the Boso data. Indeed, these values have been employ to plot the receiver operating characteristic (ROC) curve that represents the false positive rate (FPR) in the x-axis and the true positive rate (TPR) in the y-axis, at the following thresholds 0, 0.05, 0.1, 0.2, 0.3, 0.4, 0.5, 0.6, 0.7, 0.8, 0.9. Given a representation of the performance of the LSTT tests that have been done.

In addition, the area under the ROC curve (AUC), **Fig.5**, can be computed approximating the value of the definite integral that defines it, in other words, using the Trapezoidal rule (a linear function) or the Simpson rule (a quadratic one). Both raise

a value close to 1 for the two sample sets, obtaining an area of 0.874 with the first method and 0.892 with the second for the Taal's data, and 0.9 for the Trapezoidal rule and 0.91 for the Simpson one using the Boso data.

(a) Taal: ROC=0.892 (b) Boso: ROC=0.91

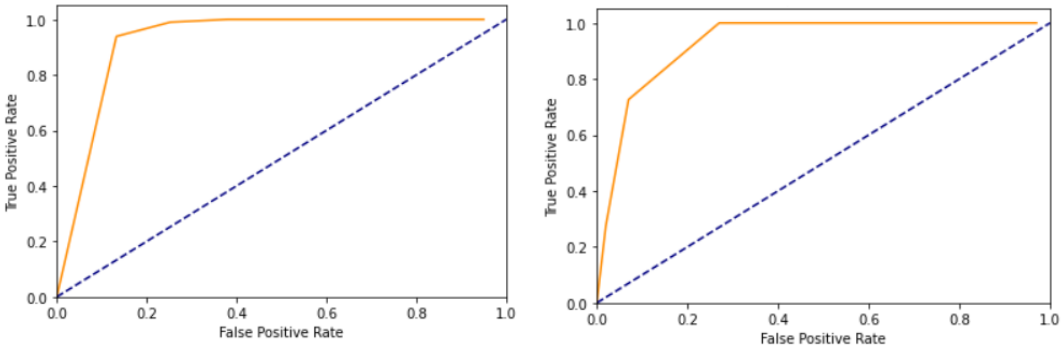

Figure 5: Receiver operating characteristic (ROC) curves computed using the LSTT outputs from the studied data sets. Made with Matplotlib library in Python.

5 Discussion

Because of atmospheric and ionospheric (in particular with L-band SAR images such as ALOS-2) disturbances, InSAR images always contain noise even if no real deformation takes place. The noise sometimes amounts to 20–30 mm to mask Earth's deformation signal if it is tiny. Also, because of the complexity of these error source, the error budget of InSAR images is also complex, and it is unlikely to be represented by simple statistics (e.g., Simons and Rosen, 2015). Therefore, discrimination of noise and deformation signals requires a comparison of the probability distribution of two samples, as we have done in this study.

Open Research Section

The data inputs used in the algorithm (InSAR filtered images and their corresponding correlation files), the LSTT code for each demo (Taal eruption and Boso gas extraction), and the synthetic data generated as a conceptual demonstration to support the interpretation of the model are available at LSTT GitHub Repository.

Acknowledgments

EM thanks the University of Tokyo Research Internship Program (UTRIP) and the Ministry of Education, Culture, Sports, Sciences and Technology (MEXT) of Japan. The UTRIP scholarship awarded by the School of Science, the University of Tokyo was instrumental in enabling the development of this study. MEXT funding made its continuation possible.

References

Anantrasirichai, N., Biggs, J., Albino, F., & Bull, D. (2019, November). The application of convolutional neural networks to detect slow, sustained deformation in insar time series. *Geophysical Research Letters*, *46*(21), 11850–11858. Retrieved from http://dx.doi.org/10.1029/2019gl084993 doi: 10.1029/2019gl084993

Balangue-Tarriela, M. I. R., Lagmay, A. M. F., Sarmiento, D. M., Vasquez, J., Baldago, M. C., Ybañez, R., ... Escudero, J. A. (2022, 03). Analysis of the 2020 taal volcano tephra fall deposits from crowdsourced information and field data. *Bulletin of Volcanology*, *84*(3), 35. Retrieved from http://dx.doi.org/10.1007/s00445-022-01534-y doi: 10.1007/s00445-022-01534-y

Bato, M. G., Lundgren, P., Pinel, V., Solidum, R., Daag, A., & Cahulogan, M. (2021, March). The 2020 eruption and large lateral dike emplacement at taal volcano, philippines: Insights from satellite radar data. *Geophysical Research Letters*, *48*(7). Retrieved from http://dx.doi.org/10.1029/2021GL092803 doi: 10.1029/2021gl092803

Beker, T., Ansari, H., Montazeri, S., Song, Q., & Zhu, X. X. (2023). Deep learning for subtle volcanic deformation detection with insar data in central volcanic zone. *IEEE Transactions on Geoscience and Remote Sensing*, *61*, 1–20. Retrieved from http://dx.doi.org/10.1109/TGRS.2023.3318469 doi: 10.1109/tgrs.2023.3318469

Brengman, C. M. J., & Barnhart, W. D. (2021, March). Identification of surface deformation in insar using machine learning. *Geochemistry, Geophysics, Geosystems*, *22*(3). Retrieved from http://dx.doi.org/10.1029/2020GC009204 doi: 10.1029/2020gc009204

Burgmann, R., Rosen, P., & Fielding, E. (2000, 05). Synthetic aperture radar interferometry to measure earth's surface topography and its deformation. *Annual*

Review of Earth and Planetary Sciences, *28*, 169-209. Retrieved from http://dx.doi.org/10.1146/annurev.earth.28.1.169 doi: 10.1146/annurev.earth.28.1.169

Farr, T. G., Rosen, P. A., Caro, E., Crippen, R., Duren, R., Hensley, S., ... Alsdorf, D. (2007, June). The shuttle radar topography mission. *Reviews of Geophysics*, *45*(2). Retrieved from http://dx.doi.org/10.1029/2005RG000183 doi: 10.1029/2005rg000183

Fukuda, J. (2018, January). Variability of the space-time evolution of slow slip events off the boso peninsula, central japan, from 1996 to 2014. *Journal of Geophysical Research: Solid Earth*, *123*(1), 732–760. Retrieved from http://dx.doi.org/10.1002/2017JB014709 doi: 10.1002/2017jb014709

Furuno, K., Kagawa, A., Kazaoka, O., Kusuda, T., & Nirei, H. (2015, November). Groundwater management based on monitoring of land subsidence and groundwater levels in the kanto groundwater basin, central japan. *Proceedings of the International Association of Hydrological Sciences*, *372*, 53–57. Retrieved from http://dx.doi.org/10.5194/piahs-372-53-2015 doi: 10.5194/piahs-372-53-2015

Gaddes, M., Hooper, A., & Albino, F. (2024, June). Simultaneous classification and location of volcanic deformation in sar interferograms using a convolutional neural network. *Earth and Space Science*, *11*(6). Retrieved from http://dx.doi.org/10.1029/2024EA003679 doi: 10.1029/2024ea003679

Hooper, A., Bekaert, D., Spaans, K., & Arıkan, M. (2012, January). Recent advances in sar interferometry time series analysis for measuring crustal deformation. *Tectonophysics*, *514–517*, 1–13. Retrieved from http://dx.doi.org/10.1016/j.tecto.2011.10.013 doi: 10.1016/j.tecto.2011.10.013

Kinoshita, Y., & Furuta, R. (2024, January). Slow slip event displacement on 2018 offshore boso peninsula detected by sentinel-1 insar time-series analysis with numerical weather model assistance. *Geophysical Journal International*, *237*(1), 75–89. Retrieved from http://dx.doi.org/10.1093/gji/ggae028 doi: 10.1093/gji/ggae028

Massonnet, D., Feigl, K., Rossi, M., & Adragna, F. (1994, May). Radar interferometric mapping of deformation in the year after the landers earthquake. *Nature*, *369*(6477), 227–230. Retrieved from http://dx.doi.org/10.1038/369227a0 doi:

10.1038/369227a0

Morishita, Y. (2021, January). Nationwide urban ground deformation monitoring in japan using sentinel-1 licsar products and licsbas. *Progress in Earth and Planetary Science*, *8*(1). Retrieved from http://dx.doi.org/10.1186/s40645-020-00402-7 doi: 10.1186/s40645-020-00402-7

Morishita, Y., Lazecky, M., Wright, T., Weiss, J., Elliott, J., & Hooper, A. (2020, January). Licsbas: An open-source insar time series analysis package integrated with the licsar automated sentinel-1 insar processor. *Remote Sensing*, *12*(3), 424. Retrieved from http://dx.doi.org/10.3390/rs12030424 doi: 10.3390/rs12030424

Nonaka, T., Asaka, T., Iwashita, K., & Ogushi, F. (2020, January). Evaluation of the trend of deformation around the kanto region estimated using the time series of palsar-2 data. *Sensors*, *20*(2), 339. Retrieved from http://dx.doi.org/10.3390/s20020339 doi: 10.3390/s20020339

Okazaki, T., Fukahata, Y., & Nishimura, T. (2021, July). Consistent estimation of strain-rate fields from gnss velocity data using basis function expansion with abic. *Earth, Planets and Space*, *73*(1). Retrieved from http://dx.doi.org/10.1186/s40623-021-01474-5 doi: 10.1186/s40623-021-01474-5

Ozawa, S., Yarai, H., & Kobayashi, T. (2019, July). Recovery of the recurrence interval of boso slow slip events in japan. *Earth, Planets and Space*, *71*(1). Retrieved from http://dx.doi.org/10.1186/s40623-019-1058-y doi: 10.1186/s40623-019-1058-y

Perttu, A., Assink, J., Van Eaton, A. R., Caudron, C., Vagasky, C., Krippner, J., ... Lube, G. (2023, April). Remote characterization of the 12 january 2020 eruption of taal volcano, philippines, using seismo-acoustic, volcanic lightning, and satellite observations. *Bulletin of the Seismological Society of America*, *113*(4), 1471–1492. Retrieved from http://dx.doi.org/10.1785/0120220223 doi: 10.1785/0120220223

Pinel, V., Poland, M., & Hooper, A. (2014, December). Volcanology: Lessons learned from synthetic aperture radar imagery. *Journal of Volcanology and Geothermal Research*, *289*, 81–113. Retrieved from http://dx.doi.org/10.1016/j.jvolgeores.2014.10.010 doi: 10.1016/j.jvolgeores.2014.10.010

Popescu, R., Anantrasirichai, N., & Biggs, J. (2025, June). Unsupervised anomaly

detection for volcanic deformation in insar imagery. *Earth and Space Science*, *12*(6). Retrieved from http://dx.doi.org/10.1029/2024EA003892 doi: 10.1029/2024ea003892

Schmidt, D. A., & Bürgmann, R. (2003, September). Time-dependent land uplift and subsidence in the santa clara valley, california, from a large interferometric synthetic aperture radar data set. *Journal of Geophysical Research: Solid Earth*, *108*(B9). Retrieved from http://dx.doi.org/10.1029/2002jb002267 doi: 10.1029/2002jb002267

Shirzaei, M., Freymueller, J., Törnqvist, T. E., Galloway, D. L., Dura, T., & Minderhoud, P. S. J. (2020, December). Measuring, modelling and projecting coastal land subsidence. *Nature Reviews Earth amp; Environment*, *2*(1), 40–58. Retrieved from http://dx.doi.org/10.1038/s43017-020-00115-x doi: 10.1038/s43017-020-00115-x

Simons, M., & Rosen, P. (2015). Interferometric synthetic aperture radar geodesy. In *Treatise on geophysics* (p. 339–385). Elsevier. Retrieved from http://dx.doi.org/10.1016/B978-0-444-53802-4.00061-0 doi: 10.1016/b978-0-444-53802-4.00061-0

Sugiyama, M., Suzuki, T., Itoh, Y., Kanamori, T., & Kimura, M. (2011, 04). Least-squares two-sample test. *Neural networks*, *24*(7), 735-51. Retrieved from http://dx.doi.org/10.1016/j.neunet.2011.04.003 doi: 10.1016/j.neunet.2011.04.003

Weiss, J. R., Walters, R. J., Morishita, Y., Wright, T. J., Lazecky, M., Wang, H., ... Parsons, B. (2020, September). High-resolution surface velocities and strain for anatolia from sentinel-1 insar and gnss data. *Geophysical Research Letters*, *47*(17). Retrieved from http://dx.doi.org/10.1029/2020GL087376 doi: 10.1029/2020gl087376

Zebker, H. A., Rosen, P. A., & Hensley, S. (1997, April). Atmospheric effects in interferometric synthetic aperture radar surface deformation and topographic maps. *Journal of Geophysical Research: Solid Earth*, *102*(B4), 7547–7563. Retrieved from http://dx.doi.org/10.1029/96JB03804 doi: 10.1029/96jb03804